Eur. Phys. J. A **11**, 357–370 (2001)

THE EUROPEAN PHYSICAL JOURNAL A

The E1 capture amplitude in $^{12}C(\alpha,\gamma_0)^{16}O$

L. Gialanella[1], D. Rogalla[1], F. Strieder[1], S. Theis[1], G. Gyürki[5], C. Agodi[4], R. Alba[4], M. Aliotta[1,a], L. Campajola[2], A. Del Zoppo[4], A. D'Onofrio[3], P. Figuera[4], U. Greife[1], G. Imbriani[2], A. Ordine[2], V. Roca[2], C. Rolfs[1,b], M. Romano[2], C. Sabbarese[3], P. Sapienza[4], F. Schümann[1], E. Somorjai[4], F. Terrasi[3], and H.P. Trautvetter[1]

[1] Institut für Physik mit Ionenstrahlen, Ruhr-Universität Bochum, Bochum, Germany
[2] Dipartimento di Scienze Fisiche, Università Federico II, Napoli and INFN, Napoli, Italy
[3] Dipartimento di Scienze Ambientali, Seconda Università di Napoli, Caserta and INFN, Napoli, Italy
[4] Laboratori Nazionali del Sud, INFN, Catania, Italy
[5] Atomki, Debrecen, Hungary

Received: 6 June 2001 / Revised version: 9 July 2001
Communicated by Th. Walcher

Abstract. An excitation function of the ground-state γ_0-ray capture transition in $^{12}C(\alpha,\gamma)^{16}O$ at $\theta_\gamma = 90^\circ$ was obtained in far geometry using six Ge detectors, where the study of the reaction was initiated in inverse kinematics involving a windowless gas target. The detectors observed predominantly the $E1$ capture amplitude. The data at $E = 1.32$ to 2.99 MeV lead to an extrapolated astrophysical S factor $S_{E1}(E_0) = 90 \pm 15$ keV b at $E_0 = 0.3$ MeV (for the case of constructive interference between the two lowest $E1$ sources), in good agreement with previous works. However, a novel Monte Carlo approach in the data extrapolation reveals systematic differences between the various data sets such that a combined analysis of all available data sets could produce a biased estimate of the $S_{E1}(E_0)$ value. As a consequence, the case of destructive interference between the two lowest $E1$ sources with $S_{E1}(E_0) = 8 \pm 3$ keV b cannot be ruled out rigorously.

PACS. 24.10.-i Nuclear-reaction models and methods – 25.40.-h Nucleon-induced reactions

1 Introduction

The capture reaction $^{12}C(\alpha,\gamma)^{16}O$ ($Q = 7.16$ MeV) takes place in the helium burning of Red Giants [1] and represents a key reaction of nuclear astrophysics. The cross-section at the relevant Gamow energy, $E_0 = 0.3$ MeV (all energies are given in the center-of-mass system, except where quoted differently), determines not only the nucleosynthesis of elements up to the iron region but also the subsequent evolution of massive stars, the dynamics of a supernova, and the kind of remnant after a supernova explosion. For definitive calculations, the cross-section $\sigma(E_0)$ must be known with a precision of at least 10% . In spite of tremendous experimental efforts over nearly 30 years [2–10], one is still far from this goal. Since $\sigma(E_0) \approx 10^{-17}$ b is far too small for direct measurement using available techniques, the measured cross-sections at higher energies must be extrapolated to E_0.

The available data indicate that $\sigma(E_0)$ is dominated by the $E1$ and $E2$ capture processes into the ^{16}O ground state (= γ_0-ray capture transition), where the two multipoles appear to be of similar importance. The $E1$ amplitude arises from the low-energy tail of a broad $J^\pi = 1^-$ resonance at $E_R = 2.42$ MeV ($\Gamma_R = 400$ keV), the high-energy tail of a $J^\pi = 1^-$ subthreshold resonance at $E_R = -45$ keV, and the low-energy tail of an unidentified background amplitude due to broad $J^\pi = 1^-$ resonances at high energies; interference effects between these $E1$ sources must also be included. The $E2$ amplitude arises predominantly from the high-energy tail of a $J^\pi = 2^+$ subthreshold resonance at $E_R = -245$ keV and the direct capture process $E2(d \to s)$, or equivalently the low-energy tails of broad $J^\pi = 2^+$ resonances at high energies. Since the capture cross-sections of the $E1$ and $E2$ multipoles have different energy dependencies, one must have an independent and precise information on the energy dependence of each multipole cross-section for a reliable extrapolation to E_0.

The $E1$ angular distribution for the γ_0-ray capture transition, $W_{E1}(\theta_\gamma) \propto \sin^2\theta_\gamma$, has a maximum at $\theta_\gamma = 90^\circ$, while the $E2$ angular distribution, $W_{E2}(\theta_\gamma) \propto \sin^2\theta_\gamma \cos^2\theta_\gamma$, is zero at $\theta_\gamma = 90^\circ$. Thus, if a detector is placed in far geometry (nearly a point-like detector) at $\theta_\gamma = 90^\circ$, it will observe only the yield of the $E1$ multipole. Of course, the price is a low detection efficiency limiting the exploitable energy range. A close inspection

[a] Alexander von Humboldt fellow
[b] e-mail: rolfs@ep3.ruhr-uni-bochum.de

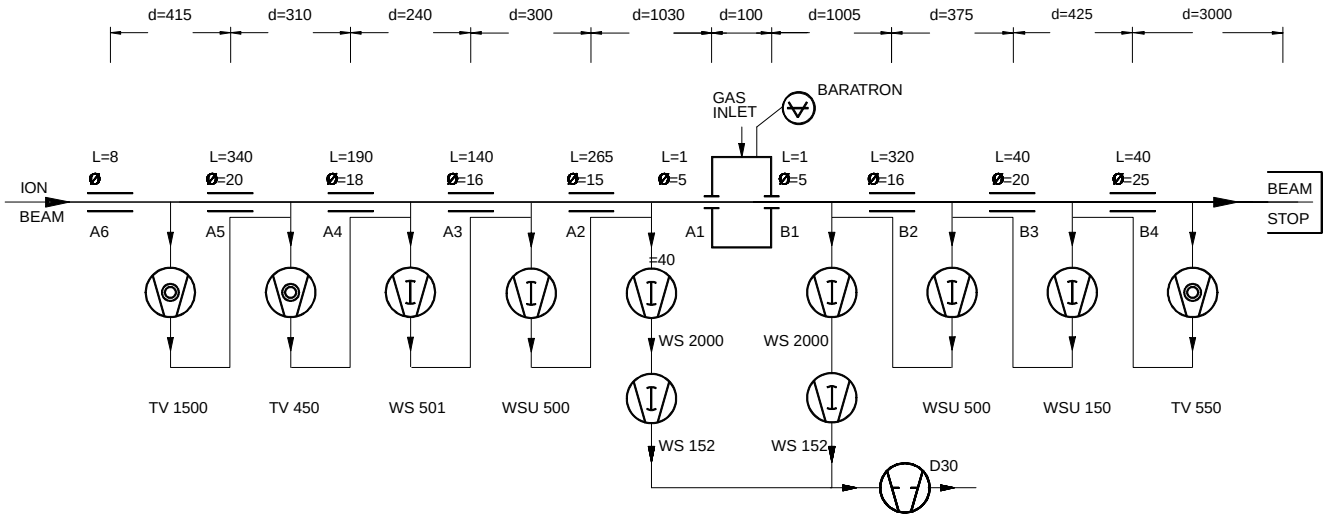

Fig. 1. Schematic diagram of the windowless gas target system. The ion beam enters and leaves the target chamber (gas cell) through a set of apertures of high pumping impedance, whose lengths (L), diameters (Φ), and mutual distances (d) are given in units of mm. The differential pumping is performed using Roots blowers (*e.g.*, WS2000, pumping speed = 2000 m^3/h) and turbo pumps (*e.g.*, TV1500, pumping speed = 1500 l/s). The target gas was fed via a regulating needle valve into the target chamber and delivered to air via a roughing pump (D30, pumping speed = 30 m^3/h), with a ^{4}He gas consumption of about 1 l/s. The gas pressure inside and outside the target chamber was measured using Baratron capacitance manometers.

of the available data for the $E1$ multipole [3,5–8,10] shows that at energies below and above the $E_R = 2.42$ MeV resonance the various data sets have systematic differences. There is only one data set [8], in which the $E1$ multipole was observed at $\theta_\gamma = 90°$ in far geometry. From the measurement of angular distributions, the $E1$ multipole was deduced in 3 data sets [5,7,10]. The other data sets were obtained in close geometry observing approximately the angle-integrated yield of the $E1$ and $E2$ multipoles, which was in turn corrected for the contribution of the $E2$ multipole; the resulting $E1$ data are thus in a way model dependent. Furthermore, the data set of [6] (using an extended gas target) did not include interference effects between the $E1$ and $E2$ multipoles which cannot be neglected at energies outside the 2.42 MeV resonance according to [8]; the effects are nearly absent for a solid target, used in the data set of [3]. Finally, to arrive at reliable $E1$ data from the summed $E1$ and $E2$ yields as in [6], the angular distributions for an extended γ-ray source must be known with high precision, as discussed in [8]. Additional $E1$ data obtained at $\theta_\gamma = 90°$ (in far geometry) with a precision of at least 10% appear thus highly desirable, which may be obtained with an array of detectors placed in a plane (perpendicular to the beam axis) around the target. Such measurements [11] are reported here, where the reaction was initiated in inverse kinematics, $^4\mathrm{He}(^{12}\mathrm{C},\gamma_0)^{16}\mathrm{O}$.

2 Equipment and set-up

The 4 MV Dynamitron tandem accelerator at the Ruhr-Universität Bochum provided a ^{12}C ion beam over the energy range $E_{lab} = 4.5$ to 14 MeV with a particle current of up to 50 μA at the target. Other ion beams (^{11}B, ^{16}O, ^{19}F) were provided for calibration and normalisation purposes. The absolute beam energy is known [12] to a precision of 4 parts in 10^4, which is sufficient for the requirements of the present work. The energy spread for ^{12}C ions was found [12] to be $\Delta E_{lab} = 2.8(1+q)$ keV at $E_{lab} = 10.5$ MeV, where q is the selected ion charge state.

A schematic diagram of the windowless gas target system is shown in fig. 1. The beam passed first through five apertures (A6 to A2, "upstream"), entered the target chamber (a cylindrical gas cell of 10 cm length with apertures A1 and B1 of $\Phi = 6$ mm diameter each), passed through another set of apertures (B2 to B4, "downstream"), and was stopped finally in a Faraday cup. The Faraday cup was located within a 1.5 m thick concrete wall and surrounded by a 0.5 m thick paraffin shield, both at a 5 m distance from the gas cell. The gas cell had ports used for gas inlet, pressure measurement, and installation of a Si detector. The gas pressure in the gas cell and in the first pumping stages was measured with Baratron capacitance manometers to an accuracy of 2% . This measurement is absolute and independent of the gas used. The gas flow through the upstream aperture A1 of the gas cell was pumped by a windowless gas-target system with five pumping stages, consisting of Roots blowers and turbo pumps [8,12]. The gas flow through the downstream aperture B1 of the gas cell was pumped by another windowless gas-target system with four pumping stages. For ^{4}He gas (99.9999% chemical purity) of 20 Torr pressure in the gas cell, the pumping systems reduced the pressure to about 0.8 Torr in the regions of the first pumping stages and to about 1×10^{-7} Torr in the region of the fifth pumping stage. A similar reduction was observed for other pressure values and target gases.

In order to minimise beam-induced background, in particular on the apertures A1 and B1 of the gas cell, the

apertures had relatively large diameters increasing in size with distance from the gas cell (fig. 1), such that the focus point of the ion beam could be placed within the gas cell. To reach this condition, the ion-beam optics was defined by the combination of 3 collimators: the first collimator ($\Phi = 25$ mm) was placed before the upstream gas-target system at a distance $z = 5.7$ m from the center of the gas cell, the second collimator ($\Phi = 2$ mm, $z = 61$ cm) was retractable — with a 0.1 mm reproducibility — from the beam axis after the focusing procedures, and the third collimator consisted of the apertures A1 and B1 of the gas cell. The ion-beam current was minimised on the collimators and maximised in the Faraday cup. The collimators together with the Faraday cup defined the angle of the incident beam to better than 0.6°. During the course of the experiments, the ion-beam optics was checked about every 3 hours. A ^{3}He proportional counter was placed near the gas cell and monitored the neutron flux in the detector region. This information was useful at the highest energies, where the ion-beam focusing included a minimisation of the neutron flux.

The yield of the elastically scattered ^{4}He recoils was observed (fig. 2) in a Si surface-barrier detector (100 μm thickness) installed at $\theta_{\rm lab} = 75°$ in the gas cell. The detector was collimated with an aperture (facing the detector) of $\Phi = 0.4$ mm at a distance $d = 164$ mm from the beam axis and with a slit of width $s = 0.4$ mm placed at a distance $f = 136$ mm from the aperture. The geometry defined the effective target length seen by the detector and its solid angle as $l_{\rm el}\Omega_{\rm lab} = \pi r^2 s(fd\sin\theta_{\rm lab})^{-1} = 2.30 \times 10^{-6}$ mm sr. The geometry defined the detection angle to a precision $\Delta\theta_{\rm lab} = 0.3°$. In order to improve the energy resolution of the detector with gas in the gas cell, the volume of its installation pipe (between the slit and the detector) was pumped at the back-side by the downstream pumping system (not shown in fig. 2). Due to the small slit width, this pumping had no significant effect on the pressure profile within the gas cell (subsect. 3.1). The elastic-scattering yield was used to monitor the product of beam intensity and target density as well as possible contaminants in both. In the case of the $^1H(^{19}F,\alpha\gamma)^{16}O$ reaction at the $E_{\rm R,lab} = 6.46$ MeV resonance (subsect. 3.10), the low-energy hydrogen recoils could not be observed in this Si detector. Thus, a second Si detector was installed near the first downstream pumping stage (fig. 2), where the pressure and thus the detection threshold were sufficiently low to observe the hydrogen recoils. The product of effective length and solid angle was here $l_{\rm el}\Omega_{\rm lab} = 5.80 \times 10^{-5}$ mm sr.

For γ-ray spectroscopy, 6 coaxial Ge detectors (GEm p-type from EG&G Ortec, relative efficiency = 70% , energy resolution = 2.2 keV at $E_\gamma = 1.2$ MeV) were installed at $\theta_\gamma = 90°$ with a mean 170 mm distance between the beam axis and the detector front face. The intrinsic crystal geometry of each Ge detector was available from the supplier and provided the basis for Monte Carlo simulations (subsect. 3.7). The detectors were placed in a plane perpendicular to the beam axis (ring-shaped geometry around the gas target), with azimuthal angles

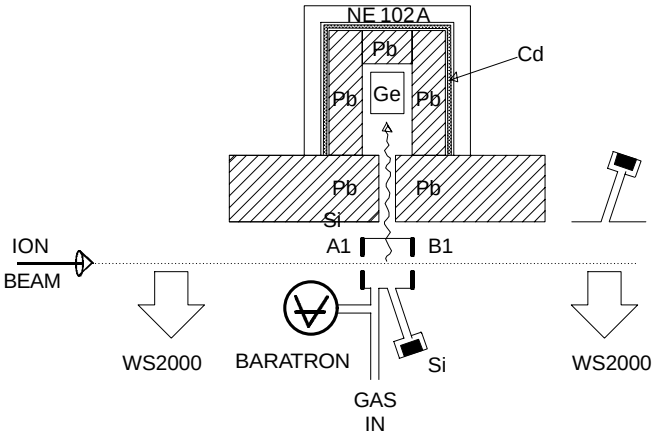

Fig. 2. Relevant parts of the gas target system near the gas cell (target chamber, with apertures A1 and B1) and the detector arrangements, where only one of six Ge detectors (at a mean distance of 170 mm from the beam axis) is shown. The Ge detectors viewed a 50 mm long distance along the beam axis within the gas cell, as defined by the Pb cylinder around the beam line. Additional passive shieldings (Pb and Cd) and active shieldings (NE102A scintillators) around the Ge detectors are also indicated. The beam intensity was monitored via the elastic-scattering yield observed at $\theta_{\rm lab} = 75°$ in Si detectors placed at the gas cell and the first downstream pumping stage.

$\varphi_\gamma = 15°$ to $165°$ relative to the horizontal axis. The detectors viewed the center of the gas cell (fig. 2), where a 12.5 cm thick cylindrical Pb shield (with a central bore hole for the beam pipe) on both sides of the gas cell defined the effective target length l_γ seen by the detectors (from geometry: $l_\gamma = 50$ mm). The background due to high-energy γ-rays and γ-rays from thermal neutron capture (neutrons created by cosmic rays or by the beam in the Faraday cup or in the gas-target apertures) was minimised using a 5 cm thick Pb wall followed by a 0.5 mm thick Cd sheet, both surrounding completely the detectors: the passive shielding. The thermal neutrons created outside the detector set-up were captured by the Cd sheet and the produced capture γ-rays were absorbed in turn by the Pb shield placed between the Cd sheet and the Ge detectors (fig. 2). The active shielding against cosmic muons consisted of 11 large-area plastic scintillators (type NE102A, 3 cm thickness) surrounding completely the passive shielding in the upper hemisphere of the detector arrangement. Coincidence events between the Ge detectors and the scintillators were rejected (see below).

The signals of all detectors were stored in an event-by-event mode for playback data analyses as described in detail elsewhere [11]. Briefly, the linear signals from the Ge detectors were stored in an analogue-to-digital converter (ADC). They were also fed into timing-filter amplifiers (TFA) followed by constant-fraction-discriminators (CFD) and a pattern unit, which allowed to identify the Ge detector producing a given linear signal. The spectrum from this pattern unit was stored in another ADC (fig. 3). In turn, the pattern spectra allowed to obtain the γ-ray

spectrum for each Ge detector in the playback data analyses by selecting events corresponding to one of the peaks labelled 1 to 6 in fig. 3. These spectra were individually calibrated (subsect. 3.5) and then summed. The signals from the CFDs of the 6 Ge detectors were processed in a logic fan-in-fan-out (LF) unit and its output was used as the start signal of a time-to-amplitude converter (TAC). The stop signal of the TAC was provided by the 11 plastic scintillators processed also in TFAs, CFDs, and a LF. The resulting TAC spectrum was stored in another ADC and used to reject coincident events between the Ge detectors and the scintillators. Another electronic system provided information on pile-up effects [11], which was also stored in an ADC. The spectra of the two Si detectors were stored in an ADC each. Furthermore, a trigger signal was generated when any of the Ge or Si detectors provided a linear signal. Every time a trigger signal was generated, all ADCs of a Canberra multiparameter data-acquisition system (DAQ) were read and a veto signal generated and kept on until all of the ADCs had finished their conversion. This feature guaranteed an equal dead time for all detectors which was independent of the respective counting rates; this independence is needed if one normalises the yield of one detector (*e.g.*, the γ-ray flux of a Ge detector) to the yield of another detector (*e.g.*, the elastic-scattering flux of a Si detector). The conversion of a signal took place if a gate signal (10 μs wide) from the DAQ arrived 360 ns before the signal passed a threshold and if no veto signal was present. The output of the ADCs was packed into an event, *i.e.* a vector with six components, and stacked in a 4 kByte buffer. When the buffer was full, it was sent to a VMS DEC Vax workstation and stored on tape. During this operation a second buffer was used; if the second buffer was full before the first buffer was empty, a veto signal to the ADCs blocked temporarily any further data acquisition.

3 Experimental procedures and results

For the measurement of an absolute excitation function in the ^{4}He(^{12}C,γ_0)^{16}O reaction, the number of capture γ-rays, N_γ, observed with the 6 Ge detectors is related to the differential cross-section $\sigma(E_\gamma,\theta_\gamma)$ of the reaction by the equation [1]

$$N_\gamma = \int\int N_\mathrm{p} N_\mathrm{t}(z)\sigma(E_\gamma,\theta_\gamma)\varepsilon_\gamma(E_\gamma,\theta_\gamma)\mathrm{d}z\mathrm{d}\Omega, \qquad (1)$$

where E_γ and θ_γ are the respective energy and emission angle of the capture γ-ray, N_p is the number of projectiles reaching the gas cell, $N_\mathrm{t}(z)$ is the density of target atoms along the beam axis, and $\varepsilon_\gamma(E_\gamma,\theta_\gamma)$ is the absolute detection efficiency of the 6 Ge detectors. The quantity $N_\mathrm{t}(z)$ is proportional to the pressure profile $Y(z)$ (subsect. 3.1),

$$N_\mathrm{t}(z) = N_\mathrm{t}(0)Y(z)/Y(0), \qquad (2)$$

where $N_\mathrm{t}(0)$ and $Y(0)$ are the density and pressure at the center of the gas cell, respectively. The z-dependence of

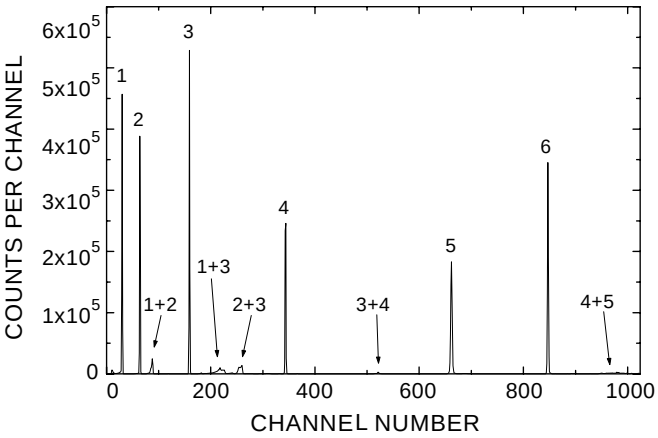

Fig. 3. Sample pattern spectrum obtained for the 6 Ge detectors: the peaks labelled 1 to 6 correspond to events from the respective Ge detectors 1 to 6. Events, for which 2 Ge detectors provided a linear signal (*e.g.*, due to Compton scattering or cascade transitions), are visible and labelled by the summed numbers of their origin; since their intensities are low, we have neglected them in the playback data analyses.

the remaining terms in eq. (1) is essentially based on the energy loss of the projectiles in the He gas, where the resulting energy E at the center of the gas cell is related to the γ_0-ray energy E_γ by $E_\gamma = E + Q$. Equation (1) can then be rewritten as

$$N_\gamma = N_\mathrm{p} N_\mathrm{t}(0)\sigma(E_\gamma)\varepsilon_\gamma(E_\gamma)l_\gamma, \qquad (3)$$

with the definition

$$\varepsilon_\gamma(E_\gamma)l_\gamma = \sigma(E_\gamma)^{-1}\int\int Y(z)Y(0)^{-1}\sigma(E_\gamma,\theta_\gamma)\varepsilon_\gamma(E_\gamma,\theta_\gamma)\mathrm{d}z\mathrm{d}\Omega. \qquad (4)$$

The product $\varepsilon_\gamma(E_\gamma)l_\gamma$ is essentially the convolution along the beam axis of the γ-ray angular distribution with the detection efficiency, which was determined using a Monte Carlo simulation (subsect. 3.7). The product $N_\mathrm{p}N_\mathrm{t}(0)$ in eq. (3) was measured via the yield N_el of the elastically scattered ^{4}He recoils concurrently observed in the Si detector at $\theta_\mathrm{lab} = 75°$ (fig. 2),

$$N_\mathrm{el} = N_\mathrm{p} N_\mathrm{t}(0)\sigma_\mathrm{el}(E,\theta_\mathrm{cm})\Omega_\mathrm{lab} l_\mathrm{el}\Omega_\mathrm{cm}/\Omega_\mathrm{lab}, \qquad (5)$$

where $\sigma_\mathrm{el}(E,\theta_\mathrm{cm})$ is the differential elastic-scattering cross-section at the center-of-mass detection angle θ_cm, and $\Omega_\mathrm{cm}/\Omega_\mathrm{lab}$ is the ratio of the center-of-mass solid angle to the laboratory solid angle. The cross-section $\sigma_\mathrm{el}(E,\theta_\mathrm{cm})$ is related to the Rutherford scattering law $\sigma_\mathrm{R}(E,\theta_\mathrm{cm})$ by a function $K(E) = \sigma_\mathrm{el}(E,\theta_\mathrm{cm})/\sigma_\mathrm{R}(E,\theta_\mathrm{cm})$, which has been measured (subsect. 3.4). The combination of eqs. (3) and (5) leads to the expression

$$\sigma(E_\gamma) = (N_\gamma/N_\mathrm{el})K_\mathrm{norm}K(E)(\varepsilon_\gamma(E_\gamma)l_\gamma E^2)^{-1}, \qquad (6)$$

where the term K_norm contains all the energy-independent constants, which in turn has been determined by comparison with a reaction of well-known cross-section (subsect. 3.10).

The accuracy of the cross-section determination depends on the precision, with which the individual parameters entering eqs. (4) to (6) can be measured.

3.1 Pressure profile

In the extended gas cell (fig. 2), the gas pressure between the apertures A1 and B1 is expected to be nearly constant and unaffected by the gas flow through these apertures. The major pressure drop should occur across these apertures, followed by a further pressure drop along the tubes connecting the gas cell with the first pumping stages, where one observes a pressure lower by a factor 25 compared to that in the gas cell. To measure this expected pressure profile, we removed the active and passive shieldings from the set-up (fig. 2) and used the narrow $E_R = 1.058$ MeV resonance ($\Gamma_R = 28$ eV) in $^4He(^{16}O,\gamma_0)^{20}Ne$ at $P(^4He) = 20$ Torr. For this pressure value and Γ_R value, the resulting thick-target γ_0-ray yield of the resonance is emitted within a length of about 0.03 mm on the beam axis, representing thus a point-like source. The flux of the $E_\gamma = 5.79$ MeV resonance γ-rays was observed with one of the Ge detectors placed at a distance of 15 cm from the beam axis. The detector was collimated —on the beam-facing side— by a 10 cm thick Pb shield with a vertical slit (20 mm width) viewing a 40 mm target length at the beam axis. The set-up was moved on a trolley parallel to the beam axis (z-axis). At each z-position, a γ-ray yield curve of the resonance was obtained [11]. Since the maximum of the yield curve corresponds to the resonance position at the center of the slit and since this yield is proportional to the gas density (pressure) at this z-position, the maximum yield values as a function of z-position correspond to the pressure profile. The yield of the ^4He recoils elastically scattered into the $\theta_{lab} = 75°$ Si detector (fig. 2) was used as a monitor in these measurements. The γ-ray flux was corrected for variation in γ-ray absorption along the z-axis. The resulting pressure profile (fig. 4) supports the above expectations leading to a full-width-half-maximum target length of $l = 101 \pm 2$ mm seen by the projectiles; the result is nearly identical with the geometrical length of the gas cell (= 100 mm). The observed yield, *i.e.* the pressure profile, has been parameterised for $P(^4He) = 20$ Torr with the function

$$Y(z) = h(1 + \exp((|z - z_0| - 0.5l)s^{-1}))^{-1} + k, \qquad (7)$$

with $h = 17.1$ Torr, $k = 2.87$ Torr, $s = 1.07$ mm, and $z_0 = -0.097$ mm; the corresponding areal target density is $n_{4He} = (6.62 \pm 0.05) \times 10^{18}$ atoms/cm^2. The observed energy shift $\Delta E = 670 \pm 67$ keV of the resonance over the length l is consistent with the calculated shift $\Delta E = 649 \pm 32$ keV from the TRIM program [13] (with a 5% error) using the above n_{4He} value.

A non-negligible energy loss was observed in the region before the gas cell: the necessary ^{16}O energy to observe the resonance at the beginning of the gas cell turned out to be $E_{lab} = 5530$ keV, *i.e.* 240 keV higher than the resonance energy. This energy difference corresponds to an areal density 2.46×10^{18} atoms/cm^2. Assuming a linear pressure drop along the pipe connecting the aperture A1 to the first pumping stage (here $P(^4He) = 0.8$ Torr), the density corresponds to a length of 420 mm, consistent with the 465 mm geometrical length of the pipe. This information together with the length l (see above) have been used also in the determination of the effective beam energy (subsect. 3.8).

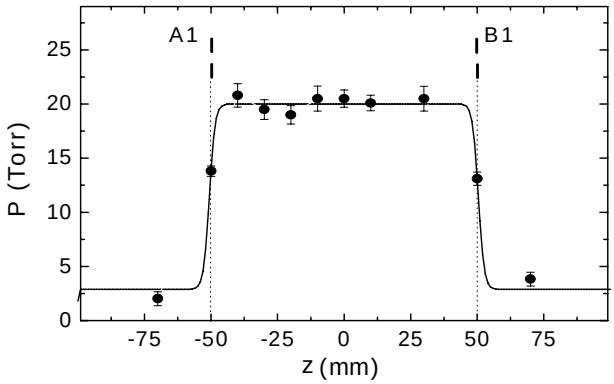

Fig. 4. Pressure profile along the beam axis for ^4He gas of 20 Torr, where the distance z is taken from the center of the gas cell. The data lead to a target length $l = 101$ mm seen by the projectiles; the geometrical distance between the apertures A1 and B1 is 100 mm. The curve through the data points represents the result of a fitted function (subsect. 3.1).

The gas pressure must include beam-heating effects in the gas, which can decrease the local pressure along the beam path. The influence of intense ion beams on the densities of quasi-static gas targets was found [14] to depend on the dissipated power in the gas. In the present work, the effects on the gas density are less than 1% and were neglected in the analyses.

3.2 Effective γ-ray target length

As discussed in sect. 2, the effective γ-ray target length l_γ seen by the 6 Ge detectors was defined by the Pb cylinder (fig. 2). For the l_γ measurement, we used again the $E_R = 1.058$ MeV resonance in $^4He(^{16}O,\gamma)^{20}Ne$ at $P(^4He) = 20$ Torr. The resulting thick-target yield curve is shown in fig. 5, where the energy scale was transformed into a length scale along the beam axis (z-axis) using energy loss values from TRIM [13]. The yield curve corresponds to the pressure profile seen by the Ge detectors leading to $l_\gamma = 66 \pm 4$ mm, in good agreement with GEANT simulations (fig. 5 and subsect. 3.7). For the case of $^4He(^{12}C,\gamma)^{16}O$, the length l_γ corresponds to a thickness $\Delta E = 60$ keV at $E = 2.0$ MeV and $P(^4He) = 20$ Torr. The pressure profile was parameterised using the same function as that given in eq. (7), with the parameter values $h = 19.7$ Torr, $k = 0.34$ Torr, $s = 2.9$ mm, and $z_0 = 0.0$ mm.

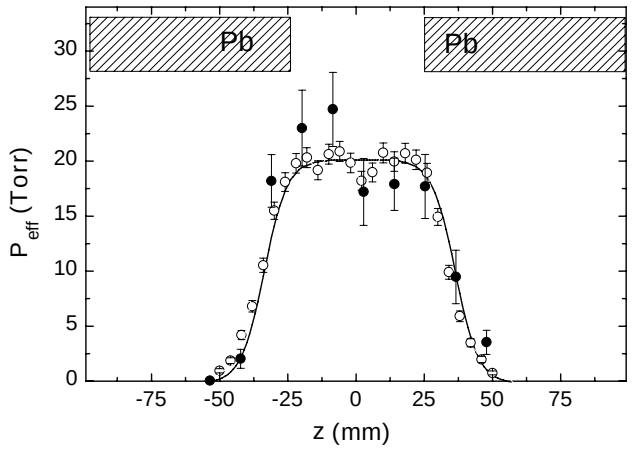

Fig. 5. Pressure profile along the beam axis for γ-ray detection in the set-up of fig. 2 (and ^{4}He gas of 20 Torr), where the distance z is taken from the center of the gas cell. The data (filled points) lead to a γ-ray target length $l_\gamma = 66$ mm seen by the 6 Ge detectors. The open points are the results of a GEANT simulation, while the curve through the points represents the result of a fitted function (subsect. 3.2). The Pb cylinders around the beam line are separated by a 50 mm wide slit, through which the Ge detectors can view the gas cell.

3.3 Mean scattering angle

Since the γ-ray data are normalised essentially to the Rutherford elastic-scattering cross-section (subsect. 3.4), an experimental determination of the mean scattering angle for the Si detectors (fig. 2) was required. If the intensity of elastically scattered projectiles (I_s) and that of recoil target nuclides (I_r) can be measured in the same detector, the intensity ratio depends sensitively on the detection angle θ_{lab},

$$I_s/I_r = \sin^2\theta_{cm}\cos^4\theta_{lab} \times(4\sin^2\theta_{lab}\sin^4 0.5\theta_{cm}\cos\theta_{lab}\cos(\theta_{cm}-\theta_{lab}))^{-1} \quad (8)$$

where this equation assumes the validity of the Rutherford scattering law. In the case of ^{12}C projectiles incident on a ^{20}Ne gas, the peaks of the projectiles and recoil nuclides were well resolved [11]. Since the height of the Coulomb barrier for the ^{12}C + ^{20}Ne system is about 10 MeV, the system should follow the Rutherford law at $E_{lab}(^{12}C) \leq$ 16 MeV. The measurements were performed at different ^{20}Ne gas pressures (0.40, 0.65, and 1.00 Torr) and different ^{12}C energies (E_{lab} = 7.0, 9.0 and 11.0 MeV). The measurements led to a mean value $\theta_{lab} = 75.0^\circ \pm 0.3^\circ$ for both Si detectors, where the error includes uncertainties in background subtraction. The error is consistent with the upper limit of 0.6° from the geometry of the collimators (sect. 2).

3.4 Normalisation of γ_0-ray yields

For the normalisation of the γ_0-ray yields, the relative number of projectiles was monitored through the observation of the elastic-scattering yield of the ^{4}He recoils at $\theta_{lab} = 75^\circ$ in the Si detector installed at the gas cell (fig. 2). In order to determine the deviations of the yields from the Rutherford scattering law, Ar gas (1 Torr) was admixed into He gas (2 Torr). The ^{12}C + ^{40}Ar system should follow the Rutherford scattering law at the relevant energies $E_{lab}(^{12}C) \leq 13$ MeV, using similar arguments as discussed above. The observed energy dependence of the ^{12}C + ^{4}He elastic-scattering yields relative to argon, for the beam energies at the center of the gas cell (subsect. 3.8), is shown in fig. 6 and numerical values are given in table 1. The results have been normalised to the Rutherford scattering cross-section at the lowest energies, where the intensity ratio approached a constant value. The data are in good agreement with previous works [4,8,9]. The observed deviations from the Rutherford scattering law —the function $K(E) = \sigma_{el}(E,\theta_{cm})/\sigma_R(E,\theta_{cm})$ (fig. 6)— are relatively small and the normalisation of the γ-ray data was corrected for the deviations.

3.5 Energy calibration, line-shape, and relative efficiency of the Ge detectors

The energy calibration of the 6 Ge detectors was performed using the E_R = 148 keV resonance in ^{1}H(^{11}B, γ)^{12}C (for $P(H_2) = 1.0$ Torr) emitting predominantly cascade γ-rays with $E_\gamma = 4.44$ and 11.67 MeV (fig. 7). The full-energy, single-escape and double-escape peaks of both γ-rays together with the 2.61 MeV RdTh background line were used for the calibration. The calibration coefficients were measured for each detector at the beginning of each beam time period: no significant change in the coefficients has been observed over a time period of four months. The experimental line-shape of the $E_\gamma = 4.44$ and 11.67 MeV γ-rays was used in Monte Carlo simulations using the program GEANT (subsect. 3.7). The resulting parameters of this simulation were involved in the calculation of the line-shape for the γ_0-ray transition in ^{4}He(^{12}C,γ)^{16}O. Finally, the cascade transitions allowed to derive the relative efficiency of the detectors at $E_\gamma = 4.44$ and 11.67 MeV (fig. 8) supporting the corresponding GEANT simulations (subsect. 3.7).

3.6 Gamma-ray background

With the passive and active shielding around the Ge detectors (fig. 2), the cosmic background in the relevant energy range E_γ = 8.5 to 10.6 MeV was reduced by a factor 20 [11]. A spectrum representing the remaining cosmic background was obtained with sufficient accuracy over a running time of 4 weeks, with the accelerator turned off. This spectrum was subtracted from every beam-induced spectrum, with a normalisation performed in the energy region E_γ = 16 to 26 MeV [11]. The resulting spectrum obtained at the lowest energy (E_{lab} = 5.80 MeV, running time = 4 weeks) is shown in fig. 9a, that near the top of the E_R = 2.42 MeV resonance (E_{lab} = 9.90 MeV, running time = 13 hours) in fig. 9b, and that at the highest energy (E_{lab} = 12.20 MeV, running time = 1 week) in fig. 9c. Due

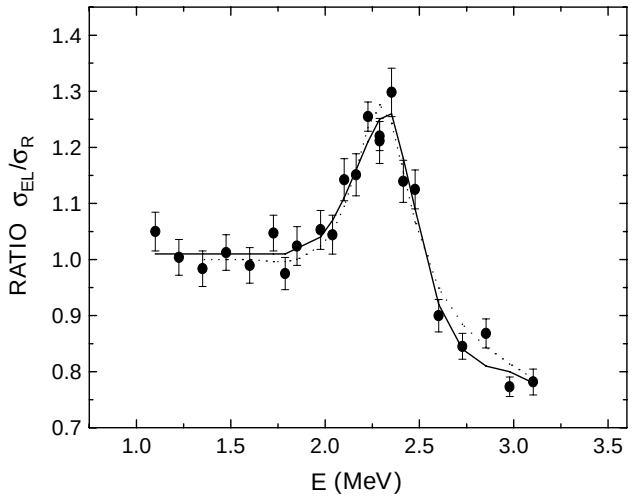

Fig. 6. Energy dependence of the elastic-scattering cross-section ($\sigma_{\rm el}$) for the ^{12}C + ^{4}He system relative to the Rutherford scattering law ($\sigma_{\rm R}$) at $\theta_{\rm lab} = 75°$. The solid line through the data points is the result of a fitted function [11], $K(E) = \sigma_{\rm el}(E,\theta_{\rm cm})/\sigma_{\rm R}(E,\theta_{\rm cm})$, and the dotted line shows the results of a previous measurement [9].

to the relatively high cross-section at the $E_{\rm R} = 2.42$ MeV resonance, the associated spectrum (fig. 9b) shows clearly the full energy peak (FEP) as well as the escape peaks (EP) and Compton edges (CE) of the γ_0-ray transition; the excellent quality of this spectrum is due to the high-energy resolution of the Ge detectors and the far geometry, which reduced the Doppler broadening. For the spectra obtained at other beam energies such as those shown in figs. 9a and 9c, only the full energy peak was clearly visible with the Ge detectors, and this FEP was superposed on a sizeable beam-induced background, in particular at high beam energies. From detailed studies it was concluded previously [8] that the major source of this background arises from local capture of neutrons created in the ^{12}C + ^{12}C fusion reactions (induced on beam-defining apertures) and that this background can be described by a smooth function without any superimposed narrow lines. The present work confirmed essentially these conclusions (see however fig. 10c). Several attempts were made in the present work to determine this background quantitatively, such as spectra obtained without gas in the gas cell and with other gases in the gas cell (Ne and Ar, at different pressures), but a satisfactory agreement with the actual spectra (such as fig. 9c) was never obtained. In view of the strong energy dependence of the background and the large uncertainty in its determination for an analysis of the complete γ_0-ray peak form (*i.e.* including FEP, SE, and CE), we analysed only the FEP of the collected spectra, for which the signal-to-background ratio is maximised. The line shape of the FEP extends only over an energy region of about 100 keV and can be described in terms of a few parameters (subsect. 3.7).

Table 1. Ratio of the experimental ^{12}C + ^{4}He elastic-scattering cross-section ($\sigma_{\rm el}$) relative to the Rutherford scattering law ($\sigma_{\rm R}$).

$E^{\rm a}$ (MeV)	$\sigma_{\rm el}$ / $\sigma_{\rm R}$
1.100	1.05 ± 0.03
1.225	1.00 ± 0.03
1.287	0.920 ± 0.017
1.350	0.98 ± 0.03
1.475	1.01 ± 0.03
1.600	0.99 ± 0.03
1.663	0.92 ± 0.03
1.726	1.05 ± 0.03
1.788	0.98 ± 0.03
1.851	1.02 ± 0.03
1.976	1.05 ± 0.03
2.039	1.04 ± 0.03
2.101	1.14 ± 0.04
2.164	1.15 ± 0.04
2.227	1.25 ± 0.03
2.289	1.21 ± 0.04
2.289	1.21 ± 0.03
2.352	1.30 ± 0.04
2.414	1.14 ± 0.04
2.477	1.13 ± 0.03
2.602	0.90 ± 0.03
2.728	0.85 ± 0.02
2.853	0.87 ± 0.03
2.978	0.773 ± 0.017
3.103	0.78 ± 0.02

[a] Effective energy (subsect. 3.8)

3.7 Monte Carlo simulations

For the calculation of γ-ray spectra obtained with the 6 Ge detectors, a Monte Carlo simulation was carried out using GEANT [15], a library of routines, which allows to describe a complex apparatus and the interaction of a large number of particles. The user has to implement routines to describe his apparatus, such as —in the present work— the extended gas target and the Ge detector arrangement (fig. 2). Briefly, in a first step one has to consider the gas pressure profile and the energy loss of the projectiles in the gas (including straggling effects), which provides a distribution of the reaction coordinates along the beam axis near the gas cell. For a given incident beam energy, one obtains thereby the reaction energy distribution along the beam axis. This distribution is then folded with the excitation curve of the reaction to obtain the effective distribution of the reaction coordinates along the beam axis. Other input information is: the internal and external geometry of the Ge detectors, the intrinsic energy resolution of the Ge detectors, the Pb shielding around the beam line defining the effective target length seen by the Ge detectors, and the stainless-steel beam line.

One important application of GEANT was the calculation of the energy dependence of the product of detection efficiency and effective target length, $\varepsilon_\gamma(E_\gamma)l_\gamma$, defined by eq. (4), which must be determined including the distri-

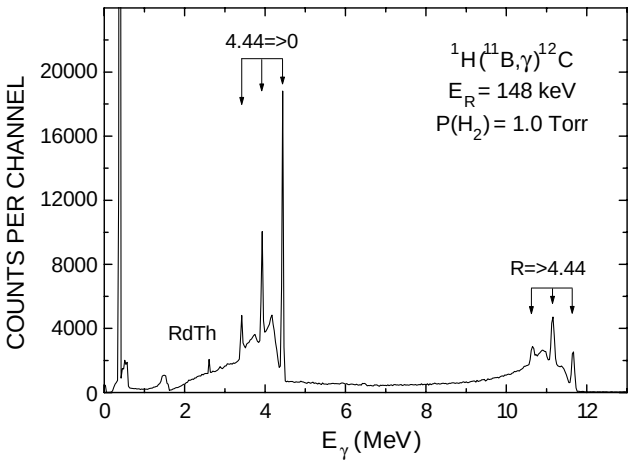

Fig. 7. Summed spectrum of the 6 Ge detectors obtained at the $E_{\rm R} = 148$ keV resonance of $^1{\rm H}(^{11}{\rm B},\gamma)^{12}{\rm C}$, which emits predominantly the cascade transitions with energies $E_\gamma = 4.44$ and 11.67 MeV.

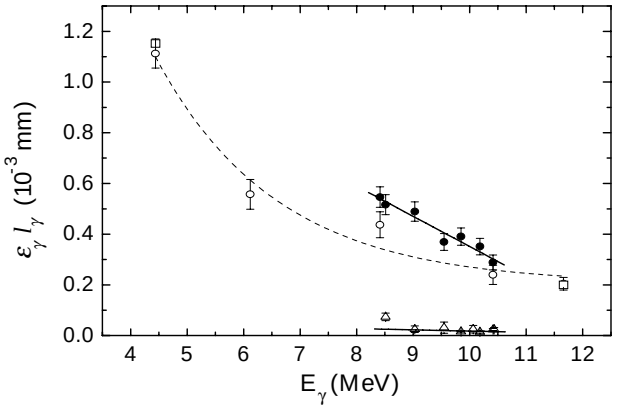

Fig. 8. Absolute value and energy dependence of the product $\varepsilon_\gamma(E_\gamma) l_\gamma$ as calculated with GEANT for different angular distributions: • = $W_{E1}(\theta_\gamma)$, ∘ = isotropy, △ = $W_{\rm E2}(\theta_\gamma)$, □ = experimental value from isotropic cascade γ-rays at $E_\gamma = 4.44$ and 11.67 MeV. The solid lines through the W_{E1}- and W_{E2}-points represent a linear fit to the calculated values, which were used for interpolation purposes. The dashed curve through the isotropy-points is to guide the eye only.

bution of the reaction coordinates and the γ-ray angular distribution. The following cases have been simulated for an extended γ-ray source:

i) isotropic angular distribution for $^1{\rm H}(^{11}{\rm B},\gamma)^{12}{\rm C}$ (E_γ = 4.44 and 11.67 MeV) and $^1{\rm H}(^{19}{\rm F},\alpha\gamma)^1$6O ($E_\gamma$ = 6.13 MeV);
ii) $W_{E1}(\theta_\gamma) \propto \sin^2\theta_\gamma$ angular distribution for $^4{\rm He}(^{12}{\rm C},\gamma)$ $^{16}{\rm O}(E_\gamma = 8.5$ to 10.6 MeV);
iii) $W_{E2}(\theta_\gamma) \propto \sin^2\theta_\gamma \cos^2\theta_\gamma$ angular distribution for $^4{\rm He}(^{12}{\rm C},\gamma)^{16}{\rm O}$ ($E_\gamma = 8.5$ to 10.6 MeV).

In the cases ii) and iii), the interference term $W_{E1E2}(\theta_\gamma) \propto \cos\theta_\gamma$ was disregarded, since its contribution is negligible near $\theta_\gamma = 90°$. Note that the $E_{\rm R} = 148$ keV resonance in $^1{\rm H}(^{11}{\rm B},\gamma)^{12}{\rm C}$ ($\Gamma = 5.8$ keV) at a pressure $P({\rm H_2}) = 1.0$ Torr and the $E_{\rm R} = 323$ keV resonance in $^1{\rm H}(^{19}{\rm F},\alpha\gamma)^{16}{\rm O}$ ($\Gamma = 2.3$ keV) at $P({\rm H_2}) = 0.10$ Torr extend both over the whole target region representing thus an extended γ-ray source. The results of the simulations are shown in fig. 8. Also shown is the experimental ratio for the 4.44 and 11.67 MeV cascade transitions in $^1{\rm H}(^{11}{\rm B},\gamma)^{12}{\rm C}$ (subsect. 3.5), normalised to the simulated value at $E_\gamma = 11.67$ MeV (square symbols in fig. 8): the good agreement provides confidence in the GEANT simulations (circular symbols in fig. 8). Due to the high computing time needed for the simulations, the product $\varepsilon_\gamma(E_\gamma) l_\gamma$ was calculated —for the $W_{E1}(\theta_\gamma)$ and $W_{E2}(\theta_\gamma)$ angular distributions— only for a few γ-ray energies in the range of interest and then interpolated for other energies (solid lines in fig. 8). For the isotropic 6.13 MeV γ-ray in $^1{\rm H}(^{19}{\rm F},\alpha\gamma)^{16}{\rm O}$ (subsect. 3.10), the simulation was performed for this energy (fig. 8).

Another important application of GEANT was the determination of the full energy peak form (FEP) for the γ_0-ray transition in $^4{\rm He}(^{12}{\rm C},\gamma)^{16}{\rm O}$ to be used in the data analysis of spectra such as those shown in fig. 9. Figure 10b shows the data points near the FEP for $E_{\rm lab} = 9.90$ MeV, where the beam-induced background was negligible; the dotted curve represents the results of the GEANT simulation for the FEP. This GEANT peak form was fitted with the function

$$F_{\rm FEP}(E_\gamma) = A_{\rm FEP}(1 + \exp((|E_\gamma - E_0| - 0.5\Gamma_{\rm FEP}) s_{\rm FEP}^{-1}))^{-1}, \quad (9)$$

where $A_{\rm FEP}$ is the height at the peak center $E_0 = E + Q$ (E = effective energy, subsect. 3.8), $\Gamma_{\rm FEP}$ is the full width at half maximum of the peak, and $s_{\rm FEP}$ determines the slope at the wings of the peak. The resulting peak form was used to fit the FEP of all spectra, where all parameters were varied again except for $s_{\rm FEP}$. It should be noted that the above peak form depends on energy in the same way as the effective pressure profile depends on the reaction coordinate (z) along the beam axis. This dependence arises from the energy loss of the beam in the gas target, the Doppler broadening, and the correlation between the reaction coordinate and the emission angle for the detected γ-rays [11]. In turn, the peak form depends also on the γ-ray angular distribution and must be determined for each reaction of interest. Finally, the background was fitted in an energy region around the FEP using the parameterisation

$$F_{\rm back}(E_\gamma) = A_{\rm back}(1 + \exp((E_\gamma - E_{\rm back}) s_{\rm back}^{-1}))^{-1} + k_{\rm back}. \quad (10)$$

In order to find suitable initial values for the fit parameters and thus to allow the minimisation routine to converge, the background parameters were first fitted in the energy region outside the FEP. The resulting background was then subtracted from the spectrum and the resulting FEP was fitted. Finally, the complete function $F(E_\gamma) = F_{\rm FEP}(E_\gamma) + F_{\rm back}(E_\gamma)$ was fitted to the whole spectrum using the initial parameters as starting values.

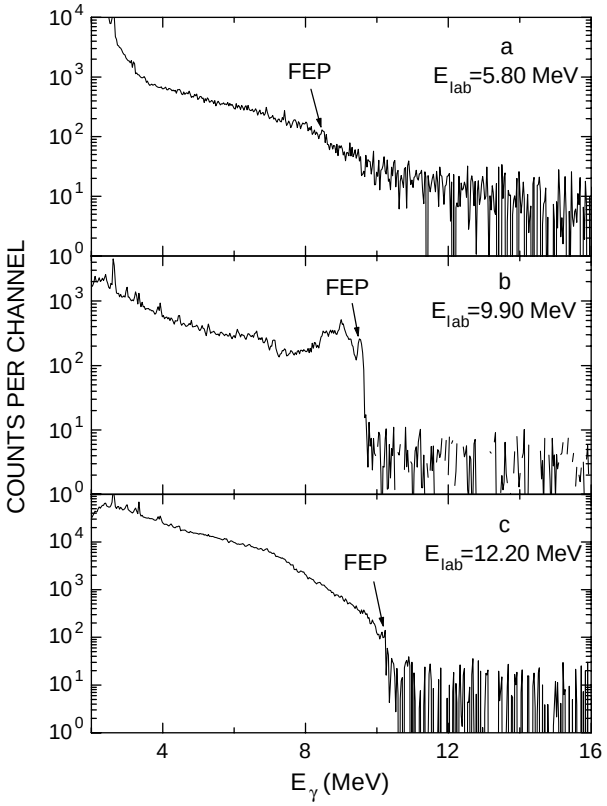

Fig. 9. Cosmic-background-subtracted spectra obtained with the Ge detector array at a) the lowest ^{12}C energy (E_{lab} = 5.80 MeV), b) near the E_R = 2.42 MeV resonance (E_{lab} = 9.90 MeV), and c) the highest energy (E_{lab} = 12.20 MeV). The full energy peak (FEP) of the γ_0-ray transition in $^4He(^{12}C,\gamma)^{16}O$ is identified, which was used in the playback data analyses.

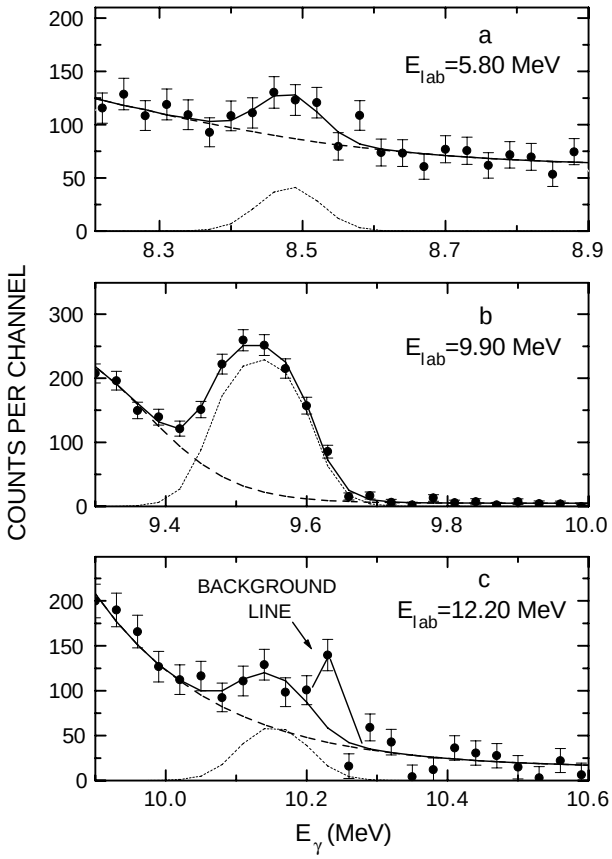

Fig. 10. Analysis of the full energy peak (FEP) for the γ_0-ray transition in $^4He(^{12}C,\gamma)^{16}O$ at a) the lowest ^{12}C energy (E_{lab} = 5.80 MeV), b) near the E_R = 2.42 MeV resonance (E_{lab} = 9.90 MeV), and c) the highest energy (E_{lab} = 12.20 MeV): dotted curve = FEP, dashed curve = background, solid curve = sum of FEP plus background. In c) a narrow background peak is visible arising from thermal neutron capture in the Ge detectors themselves.

The results of this fitting procedure are illustrated in the examples shown in fig. 10, where the dotted and dashed curves represent the FEP and background, respectively, and the solid curve their sum. In fig. 10c one can note the presence of a narrow background line near E_γ = 10.2 MeV, which was visible in all measurements above E_{lab} = 11 MeV; at these energies, a steep increase of the beam-induced neutron flux was also observed. The γ-ray line has been tentatively identified as a transition in $^{73}Ge(n,\gamma)^{74}Ge$, *i.e.* arising from thermal neutron capture in the Ge detectors themselves. Due to the high-energy resolution of the Ge detectors, this narrow background peak could be resolved from the broader $^4He(^{12}C,\gamma_0)^{16}O$ peak. The deduced error on the area of the FEP included the uncertainties of all fit parameters in the χ^2 analysis [11].

3.8 Effective beam energy

For the determination of the effective beam energy associated with the observed capture γ-ray yield, the beam energy at the center of the gas cell must be known to high accuracy. The determination requires a knowledge of the incident projectile energy and the energy loss of the projectiles in the gas-target system and gas cell to its center (subsect. 3.1). For example, at $E_{lab}(^{12}C)$ = 9.90 MeV one finds an effective energy of $E_{eff} = E = 2386 \pm 60$ keV. The effective energy was derived also from the observed energy of the γ_0 capture transition ($E = E_{\gamma 0} - Q$). For the above example, one finds $E = 2357 \pm 11$ keV, in good agreement with the value quoted. Since the γ-ray method provides directly the effective energy associated with the observed γ-ray yield and since it is independent of energy loss information as well as of the energy dependence of the cross-section, we have used this method, except at energies near the narrow E_R = 2.68 MeV resonance (fig. 11).

3.9 Suppression of the E2 capture amplitude

For a point-like detector, the $E2$ branch to the ground state ($R \to 0 : 61 \pm 4\%$ [5]) of the narrow $E_R = 2.68$ MeV resonance in $^4He(^{12}C,\gamma)^{16}O$ ($J^\pi = 2^+$) should not be visible at $\theta_\gamma = 90°$, while the nearly isotropic secondary transition 6.92 $\to$ 0 MeV of the $R \to 6.92 \to 0$ MeV cascade

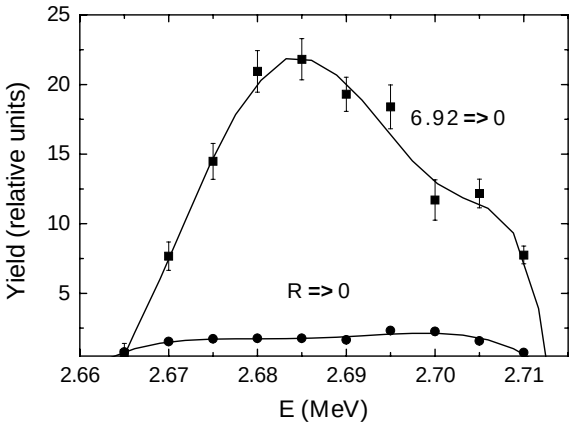

Fig. 11. Thick-target yield curves at the $E_R = 2.68$ MeV resonance of ^{4}He(^{12}C, γ)^{16}O for the $R \to 0$ MeV $E2$ transition and the (nearly isotropic) 6.92 MeV secondary transition of the $R \to 6.92 \to 0$ MeV cascade. The results lead to a suppression of the $E2$ radiation by a factor 11. The curves through the data points are to guide the eye only.

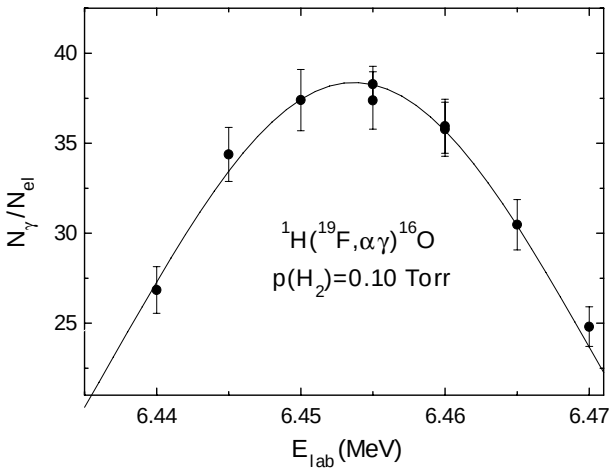

Fig. 12. Thin-target yield curve of the $E_R = 323$ keV ($E_{lab} = 6.46$ MeV) resonance in ^{1}H(^{19}F, $\alpha\gamma$)^{16}O ($E_\gamma = 6.13$ MeV) for $P(H_2) = 0.10$ Torr. The curve through the data points represents the Breit-Wigner energy dependence for the reported width $\Gamma_{R,lab} = 46$ keV [16].

(21 ± 4% [5]) should be fully visible (sect. 1). The observed thick-target yield curves (point-like sources) for the $R \to 0$ and $6.92 \to 0$ MeV transitions have been corrected for the difference in efficiency (fig. 8) and branching ratio. The results (fig. 11) lead to a suppression of the $E2$ radiation for a point-like source by a factor 11, in good agreement with GEANT (factor 9). Thus, the Ge detectors observe predominantly the $E1$ capture amplitude, while the $E2$ capture amplitude makes only a small contribution to the observed γ_0-ray yield. For an extended γ-ray source, such as prevailing at most energies in ^{4}He(^{12}C, γ)^{16}O, the GEANT simulation leads to an $E2$ suppression by a factor 16 (fig. 8).

3.10 Absolute cross-section

The absolute cross-section σ_C of ^{4}He(^{12}C, γ)^{16}O at the center-of-mass energy $E = E_C$ was measured relative to the well-known cross-section $\sigma_F = 88 \pm 3$ mb [16] of ^{1}H(^{19}F, $\alpha\gamma$)^{16}O at $E = E_F = 323$ keV (resonance width $\Gamma_{cm} = 2.3$ keV or $\Gamma_{lab} = 46$ keV), where we use the index C and F to identify parameters of the two reactions. The cross-section σ_C is then given by the equation [11]:

$$\sigma_C(E_C) = \sigma_F(E_F)(N_\gamma/N_{el})_C(N_\gamma/N_{el})_F^{-1} \times(\varepsilon_\gamma(E_\gamma)l_\gamma)_F(\varepsilon_\gamma(E_\gamma)l_\gamma)_C^{-1}(\sigma_{el})_C(\sigma_{el})_F^{-1}, \quad (11)$$

where the individual parameters have been determined in the following way:

i) the yield ratio of the capture γ-rays (N_γ from the FEP) and elastically scattered ^{4}He recoils (N_{el}) at $E_C = 2.365$ MeV was measured in 7 different runs leading to a weighted mean $(N_\gamma/N_{el})_C = (4.26 \pm 0.13) \times 10^{-4}$;
ii) an excitation function of the 6.13 MeV γ-ray (FEP) from ^{1}H(^{19}F, $\alpha\gamma$)^{16}O in the energy region of the $E_F = 323$ keV ($E_{lab} = 6460$ keV) resonance with $P(H_2) = 0.10$ Torr is shown in fig. 12; the data were normalised to the elastic-scattering yield of the ^{1}H recoils observed in the 75° Si detector located at the first downstream pumping stage (fig. 2); the maximum of the thin-target yield curve is at $E_{lab} = 6453 \pm 3$ keV, in good agreement with the resonance value; at higher ^{19}F energies the ratio of number of counts in the two Si detectors (fig. 2) was observed to be 0.98 ± 0.03, consistent with their products $l_{el}\Omega_{lab}$ together with the pressure gradient at the two locations; the resulting yield ratio —in terms of the Si detector at the gas cell— is $(N_\gamma/N_{el})_F = 38.9 \pm 0.9$;
iii) the ratio of the product of efficiency and length for the two reactions, $(\varepsilon_\gamma(E_\gamma)l_\gamma)_F/(\varepsilon_\gamma(E_\gamma)l_\gamma)_C$, was calculated with GEANT (fig. 8) leading to a value of 1.37 ± 0.14;
iv) the ratio of the elastic-scattering cross-sections $(\sigma_{el})_C/(\sigma_{el})_F = (4.08 \pm 0.13) \times 10^{-2}$ was derived from the Rutherford scattering cross-section including the function $K(E_C = 2.365\,\text{MeV}) = 1.23$ (fig. 6).

The resulting absolute cross-section is $\sigma_C = 54 \pm 6$ nb at $E_C = 2.365$ MeV, in fair agreement with previous works ([3] = 37 ± 2 nb, [4] = 53 ± 4 nb, [5] = 46 ± 6 nb, [10] = 45 ± 5 nb). This value was used as standard for the excitation function of ^{4}He(^{12}C, γ)^{16}O, displayed in fig. 13 and given numerically in table 2 in form of the astrophysical $S(E)$ factor defined by the equation [1]

$$\sigma(E) = S(E)E^{-1}\exp(-2\pi\eta)\,, \quad (12)$$

where $2\pi\eta$ is the Sommerfeld parameter.

4 Discussion

As discussed in sect. 1, the $E1$ amplitude arises from the low-energy tail of the broad $J^\pi = 1^-$ resonance at

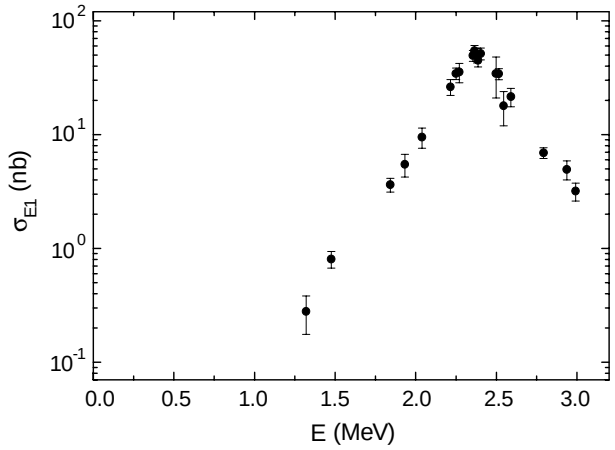

Fig. 13. Absolute cross-section $\sigma(E)$ for the $E1$ capture amplitude in $^4He(^{12}C,\gamma)^{16}O$ from the present work.

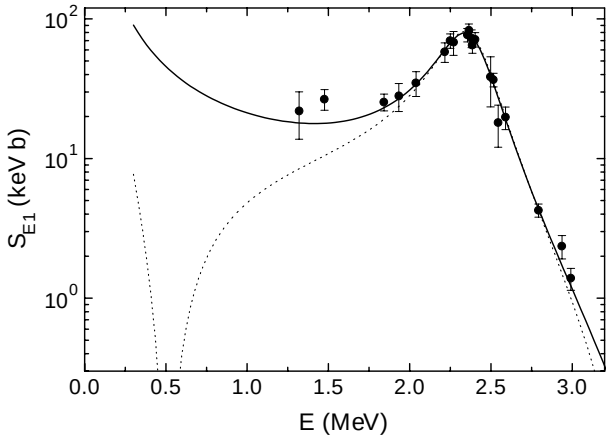

Fig. 14. The astrophysical $S(E)$ factor for the $E1$ capture amplitude from the present work. An R-matrix fit of the data together with other data [17,18] is shown for the case of constructive (solid curve) and destructive (dotted curve) interference between the broad resonance at $E_R = 2.42$ MeV ($\Gamma_R = 400$ keV) and the high-energy tail of the subthreshold resonance at $E_R = -45$ keV.

Table 2. Results for the γ_0 capture transition in $^4He(^{12}C,\gamma)^{16}O$.

E^a (MeV)	S_{E1}^b (keV b)
1.320	0.28 ± 0.10
1.476	0.80 ± 0.13
1.842	3.6 ± 0.5
1.933	5.4 ± 1.2
2.039	9.4 ± 1.9
2.216	26 ± 4
2.250	34 ± 4
2.270	35 ± 7
2.355	49 ± 5
2.365	54 ± 1.6^c
2.381	49 ± 7
2.386	45 ± 6
2.403	51 ± 6
2.498	34 ± 13
2.516	34 ± 4
2.545	18 ± 6
2.590	21 ± 4
2.793	6.9 ± 0.7
2.937	4.9 ± 0.9
2.992	3.2 ± 0.6

[a] Effective energy (subsect. 3.8)

[b] The quoted uncertainties represent statistical errors on the relative yield curve only.

[c] Absolute value measured relative to $^1H(^{19}F,\ \alpha\gamma)^{16}O$ with a normalisation error of 9% (subsect. 3.10), which is common to all data points.

$E_R = 2.42$ MeV ($\Gamma_R = 400$ keV), the high-energy tail of the $J^\pi = 1^-$ subthreshold resonance at $E_R = -45$ keV, and the low-energy tail of an unidentified background amplitude due to broad $J^\pi = 1^-$ resonances at high energies; interference effects between these $E1$ sources must also be included. The γ_0-ray $E1$ capture data ([3,5–8,10] and present work) together with data from the $^{12}C + {}^4He$ elastic scattering [17] and the α-spectrum from the β-delayed decay of ^{16}N [18] were analysed using an R-matrix formalism ([18] and references therein), whereby the χ^2 minimisation was performed using the routine MINUIT [19]. In the following discussions we will refer to the interference between the $E_R = -45$ keV and 2.42 MeV $E1$ sources, *i.e.* constructive or destructive interference effects at energies between the two resonances, as "interference between the two 1^- states".

The fitting procedures adopted closely follow that adopted in ref. [18]. One of the parameters in the fits is the interaction radius a [18], which we found to be close to 6 fm for all γ_0-ray $E1$ data sets; we have adopted therefore a value $a = 6.0$ fm for all subsequent analyses, and an uncertainty of ± 0.5 fm for the error propagation. The free parameters in the fit are the same as in ref. [18]. The input data for each fitting procedure are the γ_0-ray $E1$ capture excitation function points, the β-delayed α-particle spectra following ^{16}N decay and the elastic-scattering phase shifts. Statistical errors only were used for the fitting, while normalisation errors were propagated for the evaluation of uncertainties affecting the fit parameters, and then the $S_{E1}(E_0)$ value.

An analysis of all γ_0-ray $E1$ data sets ([3,5–8,10] and present work) and other data [17,18] favour clearly the case of constructive interference between the two 1^- states [11]: $\chi^2_{min} = 333$ and 406 (degrees of freedom $F = 269$) for constructive and destructive interference, respectively. The same conclusion is reached when only the γ_0-ray $E1$ data from the present work and other data [17, 18] are used (fig. 14; $\chi^2_{min} = 175$ and 187 ($F = 165$) for constructive and destructive interference, respectively) leading to an extrapolated value $S_{E1}(E_0) = 90$ keV b at $E_0 = 0.3$ MeV (see, however, below).

In order to evaluate the uncertainty of the extrapolated $S_{E1}(E_0)$ value, taking properly into account the experimental uncertainties, and the statistical significance

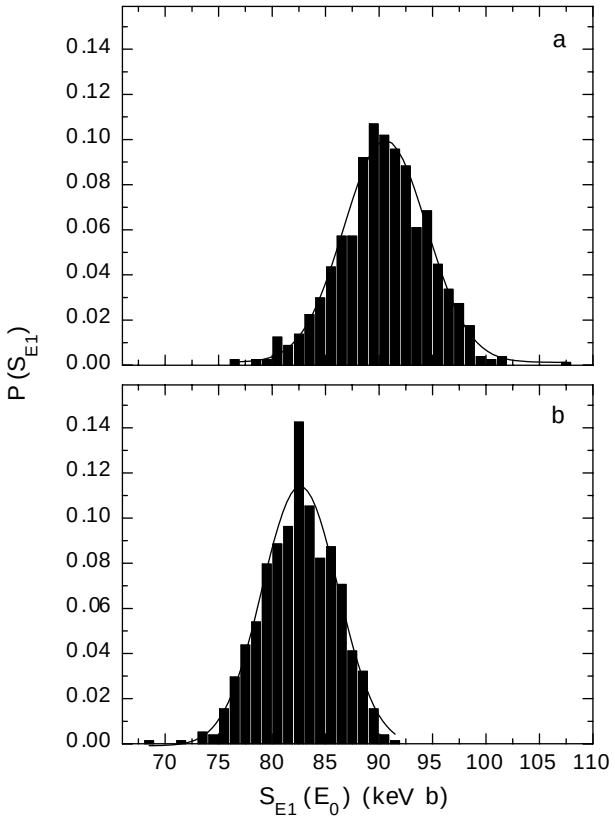

Fig. 15. Probability distribution of $S_{E1}(E_0)$ for the case of constructive interference between the two 1^- states using a) the γ_0-ray $E1$ data from the present work and other data [17, 18] and b) all γ_0-ray $E1$ data sets ([3,5–8,10] and present work) and other data [17,18]. The solid curve represents a Gaussian fit to each distribution.

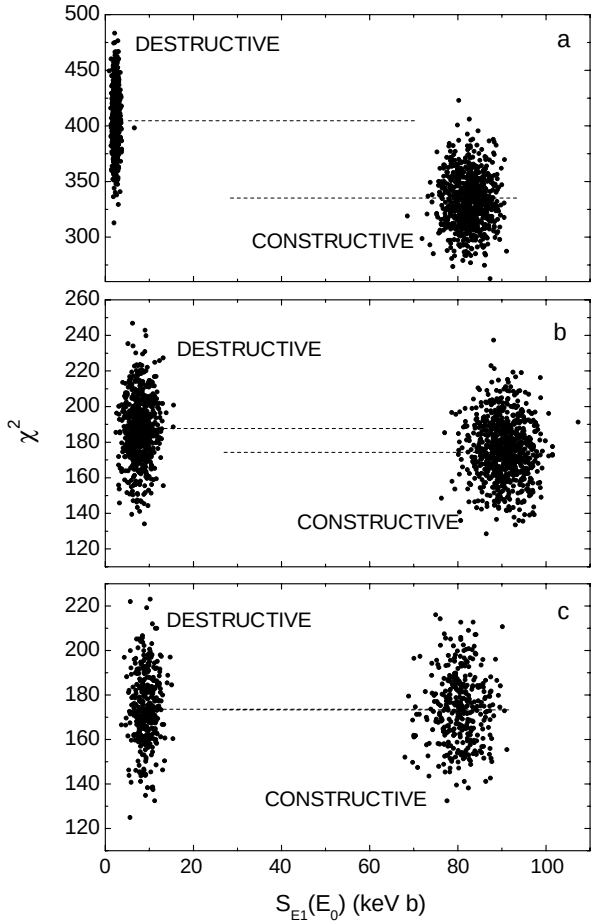

Fig. 16. Distribution of fits in the χ^2-$S_{E1}(E_0)$ plane (unnormalised χ^2 values) depending on the cases for constructive and destructive interference between the two 1^- states: a) all γ_0-ray $E1$ data ([3,5–8,10] and present work) and other data [17,18]; b) γ_0-ray $E1$ data from the present work and other data [17, 18], c) γ_0-ray $E1$ data from [6] and other data [17,18]. All data show an appreciable overlap in the χ^2 values for both signs of the interference.

of the comparison of the qualities of the fit for constructive and destructive interference, we have followed a novel approach [11].

The basic idea is that the error on $S_{E1}(E_0)$ is connected by means of the R-matrix fit function to the errors of the single data points, where the error of each single data point follows a probability distribution, *e.g.* a Gaussian distribution, whose standard deviation represents the quoted error. If one uses a set of data points to estimate the value of the fit parameters, these will follow also a probability distribution resulting from the probability distribution of the data points and the R-matrix fit function. The $S_{E1}(E_0)$ value will then follow a probability distribution that one obtains by the convolution of the probability distribution of the fit parameters. The associated multiple integration is difficult to perform, but the Monte Carlo method can provide reliable estimates. In practice, the R-matrix fit can be initiated repeatedly, where for every calculation the set of input data points is given by a random sample extracted from the experimental data statistical distribution. Using a multidimensional Gaussian distribution with the experimental results as mean values and the experimental errors as standard deviations, by means of a routine based on the Box and Mueller method [20], the probability distribution of the fit parameters is obtained, which in turn yields the distribution of the $S_{E1}(E_o)$ value.

The implementation of the method for a complete statistical analysis should include the correlation among input data arising from the common normalisation (for a given data set or, eventually, between different ones). This will be the object of a forthcoming paper [21]. We report here the results of a preliminary application, which does not include the normalisation uncertainties in the fit procedure. This can introduce a bias in the extracted fit parameters, both because of their influence on the relative weights of the different sets of data points and because the correlation among the input data is neglected.

Applying this procedure to all γ_0-ray $E1$ data sets ([3,5–8,10] and present work) and other data [17,18] and assuming constructive interference between the two 1^- states, one arrives at the probability distribution for $S_{E1}(E_0)$ illustrated in fig. 15 leading to $S_{E1}(E_0) = 82 \pm 4$ keV b at the level of one standard deviation. Adding an

Table 3. Extrapolated $S_{E1}(E_0)$ value for the case of constructive and destructive interference between the two 1^- states, for different γ_0-ray data sets together with other data [17,18].

Ref.	Constructive interference		Destructive interference			
	$S_{E1}(E_0)$ (keV b)	χ^2	$S_{E1}(E_0)$ (keV b)	χ^2	F	$\frac{\lvert F-\chi^2\rvert}{(2F)^{1/2}}$
[3]	81 ± 13	195	6 ± 3	219	169	1.3
[5]	87 ± 13	194	5 ± 3	223	171	1.2
[6]	80 ± 13	174	9 ± 3	174	154	1.1
[7]	86 ± 13	169	6 ± 3	187	154	0.8
[8]	86 ± 14	174	9 ± 3	176	159	0.8
[10]	84 ± 14	174	6 ± 2	180	165	0.5
present	90 ± 15	175	8 ± 3	187	165	0.5
all	82 ± 16	333	2.4 ± 1.0	406	269	2.8

error of 6 keV b given by the uncertainty in the branching ratio of the ^{16}N decay [18], an error of 2 keV b due to the uncertainty in the interaction radius, and an error of 4 keV b as an external error due to different absolute scales, one arrives at $S_{E1}(E_0) = 82 \pm 16$ keV b, in good agreement with the value 79 ± 21 keV b quoted previously [18]. If only the present data and those of [17,18] are used in the procedure, the result (fig. 15) is similar: $S_{E1}(E_0) = 90 \pm 16$ keV b. One might thus conclude that the $E1$ capture amplitude is rather well constrained by the available data.

However, the procedure adopted allows a closer inspection of the different γ_0-ray $E1$ data, leading to a different picture. Figure 16 illustrates the distribution of fits in the χ^2-$S_{\rm E1}(E_0)$ plane depending on the cases for constructive and destructive interference between the two 1^- states, and table 3 summarises the results of all individual data sets as well as their combination. It is interesting to note that in the case of constructive interference, the extrapolated value of $S_{E1}(E_0)$ for the combined data sets fit is within the range defined by the fits to the single data sets, while this does not hold for constructive interference. This might indicate a much stronger effect of neglecting the correlation between the data points of each data set in the case of destructive interference. However, although the combined analysis of all γ_0-ray $E1$ data suggests a preference for the case of constructive interference over that of destructive interference, the individual γ_0-ray $E1$ data do not support uniquely this conclusion: for three data sets ([6,8,10] and present work) both interference signs are equally valuable, while only two data sets [3,5] favour the case of constructive interference. All data show an appreciable overlap in the χ^2 values for both signs of the interference. The evident presence of systematic differences between the various γ_0-ray $E1$ data sets (sect. 1) may suggest that a combined fit using all available data can produce a biased estimate of $S_{E1}(E_0)$, probably related to the fact that the normalisation error is not included in the original data points. For the constructive interference case, for example, this is also indicated by the data shown in the last column of table 3. Here the ratio of the difference between the χ^2 value and the number of degrees of freedom, normalised to the expected χ^2 standard deviation $(2F)^{1/2}$ is reported. All values corresponding to individual data sets show differences smaller than 1.3 $\sigma_{\chi 2}$, while the combined fit shows a deviation of about 2.8 $\sigma_{\chi 2}$. This problem will be avoided when the normalisation error will be included in the input data statistical distribution.

In any case, it appears difficult that, with the present data, a conclusion about the sign of the interference between the two 1^- states can be definitively drawn, since the original data —in particular the analysis of the background in the energy region of the γ_0-ray transition (*e.g.*, fig. 10)— are not available for all data sets and therefore it is not possible to investigate and correct the systematic differences between them. Most likely, one has to await the results of new experiments, in which the background is eliminated to a large extent. This aim can possibly be achieved using a recoil separator to detect the ^{16}O recoils of ^{4}He(^{12}C,γ)^{16}O and a γ-ray detector array to observe the capture γ-rays, where γ-^{16}O coincidences could provide clean spectra (*e.g.*, [22] and references therein). Such γ-^{16}O coincidence data could be extended possibly to higher energies than presently performed (*e.g.*, up to $E = 5.0$ MeV), whereby such data could provide stringent constraints on the $E1$ background amplitude (see above).

The authors thank R.E. Azuma (Toronto) for provision of the R-matrix code and other advices given, K. Brand and the associated technical staff (tandem laboratory at Bochum) for providing a high current ^{12}C ion beam over long periods of time, and N. Marquardt (Dortmund) for the loan of pumps. This work was supported in part by the DAAD (Vigoni), DFG (Ro429/35-1), INFN and OTKA (T 034259).

References

1. C. Rolfs, W.S. Rodney, *Cauldrons in the Cosmos* (University of Chicago Press, 1988).
2. R.J. Jaszczak, J.H. Gibbons, R.L. Macklin, Phys. Rev. C **2**, 2452 (1970).
3. P. Dyer, C.A. Barnes, Nucl. Phys. A **233**, 495 (1974).
4. K.U. Kettner et al., Z. Phys. A **308**, 73 (1982).
5. A. Redder et al., Nucl. Phys. A **462**, 385 (1987).
6. R.M. Kremer et al., Phys. Rev. Lett. **60**, 1475 (1988).
7. J.M.L. Ouellet et al., Phys. Rev. C **54**, 1982 (1996).

8. G. Roters et al., Eur. Phys. J. A **6**, 451 (1999).
9. D. Rogalla, Diplomarbeit, Ruhr-Universität Bochum (1997).
10. R. Kunz et al., Phys. Rev. Lett. **86**, 3244 (2001).
11. L. Gialanella, Thesis, Ruhr-Universität Bochum (2000).
12. H.W. Becker et al., Z. Phys. A **351**, 453 (1995).
13. J.P. Biersack, J.F.Ziegler, *Transport of Ions in Matter, TRIM program Version 95.06* (IBM Research, New York, 1995).
14. J. Görres et al., Nucl. Instrum. Methods **177**, 295 (1980).
15. GEANT Monte Carlo program, CERN library (1993).
16. H.W. Becker et al., Z. Phys. A **305**, 319 (1982).
17. R. Plaga et al., Nucl. Phys. A **465**, 291 (1987).
18. R.E. Azuma et al., Phys. Rev. **50**, 1194 (1994).
19. MINUIT, *Function Minimisation and Error Analysis*, CERN program library (1993).
20. B.R. Bevington, D.K. Robinson, *Data Reduction and Error Analysis for the Physical Sciences* (McGraw-Hill, 1992).
21. L. Gialanella et al., work in preparation.
22. D. Rogalla et al., Eur. Phys. J. A **6**, 471 (1999).